Passivity-Based Design of Frequency Adaptive Repetitive Controller for *LCL*-Type Grid-Connected Inverters

Ying Zhao, Chuan Xie, *Senior Member, IEEE*, Chao Peng, and Jianxiao Zou, *Member, IEEE*

***Abstract*—The frequency adaptive repetitive controller (FARC) can offer high control accuracy for grid-connected inverters (GCIs) in the presence of grid voltage distortions and frequency variations. The conventional design guidelines for FARC are primarily based on the system's closed-loop transfer function, which is only able to assess the internal stability of GCIs. However, their external stability is uncertain in complex grid impedance conditions, such as a weak inductive grid, a capacitive grid, or a grid comprising multiple inverters. The frequency-domain passivity theory offers a sufficient stability condition for GCIs operated in complex grid impedance conditions and has been widely recognized and applied in the control design. This article establishes an optimization problem with constraints of internal stability condition, passivity compliance, and grid frequency variation for FARC-controlled *LCL*-type GCIs involving inverter-side or grid-side current control modes. By solving the established optimization problem, the system can fulfill a full-frequency passive output admittance, simultaneously achieving sufficient stability condition and high control accuracy regardless of grid voltage distortions, impedance and frequency variations. Finally, theoretical findings are verified by experimental results from a laboratory prototype.**

***Index Terms*—Frequency adaptivity (FA), passivity, repetitive control (RC), robustness, stability.**

I. Introduction

HIGH-GAIN current controllers have the advantage of high control accuracy and thus have gained popularity in grid-connected inverters (GCIs) that are required to comply with mandatory power quality requirements of the grid code [1], [2]. As one of the high-gain controllers, the repetitive controller (RC), with the advantages of simple structure and easy implementation, has been widely applied to different applications, e.g., uninterrupted power supplies [3], active power filters (APFs) [4], and renewable energy generations [5], [6], etc. With the increasing penetration of renewable energy sources and the high proliferation of GCIs in the grid, the grid has faced a paradigm shift from the traditional centralized generation to distributed generation. Hence, the running environment of GCIs is undergoing dramatic changes, such as wide frequency variations (e.g., 47.5–52 Hz [7]) and grid impedance variations [8], which severely aggravate the power quality and stability issues of GCIs.

One well-known deficiency of RC is that its performance is highly susceptible to grid frequency variations [9]. Researchers have proposed a variety of methods to cope with the frequency adaptivity issue of RC, which roughly fall into two categories, viz., variable sampling frequency [9], [10], [11] and fixed sampling frequency [12], [13], [14], [15], [16], [17], [18], [19], [20], [21]. With the variable sampling frequency, the ratio of the sampling frequency to the grid frequency is an integer, which serves as a prerequisite for maintaining the high performance of RCs [9]. However, a variable sampling frequency will not only compromise the overall closed-loop stability but also significantly increase the control systems' real-time implementation complexity, such as unique capabilities of the CPU for variable sampling and online controller redesign for maintaining system stability [10], [11]. With fixed sampling frequency, noninteger delay, also named the fractional delay, approximated by a finite impulse response (FIR) filter [13], [14], [15], or an infinite impulse response (IIR) filter [12], [16] or compensated by a linear-phase-lead low-pass filter (LPF) [17], has been developed for different applications. However, these fractional-delay approximation-based frequency adaptivity approaches cannot be applied to some particular scenarios, such as selective harmonic RC [19]. Hence, the virtual delay unit concept with fixed sampling frequency was developed in [19], [20], and [21], which enables the virtual variable sampling control to cope with the frequency adaptability issue of RC. The virtual delay unit is based on linear interpolation and needs to replace each delay element of RC, hence significantly increasing the computation burden.

Although many achievements have been achieved in dealing with the frequency adaptability issue of RC, primary contributions are focused on the modifications of the internal model, except for the design guidelines. The design guidelines are almost

Manuscript received 20 July 2023; revised 13 October 2023 and 5 December 2023; accepted 21 December 2023. Date of publication 28 December 2023; date of current version 16 February 2024. This work was supported in part by the National Natural Science Foundation of China under Grants 51807021 and 52107181, and in part by the Science and Technology Planning Project of Sichuan Province under Grant 2022YFG0147. Recommended for publication by Associate Editor A. Kuperman. *(Corresponding authors: Chuan Xie; Chao Peng.)*

Ying Zhao is with the School of Automation Engineering, University of Electronic Science and Technology of China, Chengdu 611731, China (e-mail: y.zhao@std.uestc.edu.cn).

Chuan Xie, Chao Peng, and Jianxiao Zou are with the School of Automation Engineering and Shenzhen Institute for Advanced Study, University of Electronic Science and Technology of China, Chengdu 611731, China (e-mail: c.xie@uestc.edu.cn; pengchao@uestc.edu.cn; jxzou@uestc.edu.cn).

Color versions of one or more figures in this article are available at https://doi.org/10.1109/TPEL.2023.3347723.

Digital Object Identifier 10.1109/TPEL.2023.3347723

based on the system's closed-loop transfer function, which can only assess the internal stability of an individual GCI connecting to an ideal inductive grid [22]. However, when GCIs operate in a complex grid, such as an inductive weak grid, a capacitive grid, or a grid comprising multiple inverters, the interactive stability between them, also called external stability, is unknown.

The external stability of the GCI system is related to the grid impedance, which can be assessed by applying the Nyquist rule to the impedance ratio of the GCI system and the grid [8], where the information about the grid impedance must be known [23], [24]. Hence, the external stability of the GCI system still cannot be ensured when the grid impedance varies. Fortunately, the frequency-domain passivity theory can guarantee the external stability of the GCI even without knowing the specific information of grid impedance [25] and gains much research attention [26], [27], [28]. According to the frequency-domain passive theory, an internally stable GCI system can always maintain its external stability in case the output admittance of the GCI is passive (i.e., the real part of the output admittance is nonnegative) [26] when it is operating in a resistive–inductive–capacitive (*RLC*) type grid, regardless of its complexity. Extensive research has been devoted to the field of passivity enhancement for GCIs, including inverter-side current control (ICC) mode [26], [29] and grid-side current control (GCC) mode [25], [27], [28], [30]. In most literature concerning the passivity enhancement for GCI's output admittance, proportional-integral and proportional-resonant (PR) controllers are commonly used [25], [26], [27], [28], [29], [30]. High-gain current controllers, such as resonators or RC, will create zeros in the output admittance of the GCI system and thus result in a risk of emerging negative-real-part regions that may trigger system oscillations. Passivity compliance design methods for the resonators [31] and RC [22] have been introduced to address their external stability issues. However, the method in [22] suffers from empirical and trivial trial-and-error. Besides, the effect of grid frequency variations and the frequency adaptive mechanism on the passivity has yet to be considered.

In light of this, the external stability issue of FARC-controlled *LCL*-type GCI in the presence of both grid impedance and frequency variations is deeply investigated in this article from the perspective of passivity stability. The main contributions can be summarized as follows.

1) A general admittance model for the FARC-controlled *LCL*-type GCI with ICC or GCC modes is built for passivity property analysis and control design. The analysis reveals that grid frequency variations and the frequency adaptive mechanism of FARC may raise the negative conductance in the GCI's output admittance, which may excite the system oscillations.
2) Passivity constraint is introduced to the design of FARC. Compared to passivity-based RC design guidelines invented in [22], this article establishes an optimization problem to replace the empirical and trivial trial-and-error. Furthermore, the grid frequency variation constraint is added to the optimization problem to ensure the passivity robustness of GCI's output admittance against the grid frequency variation.

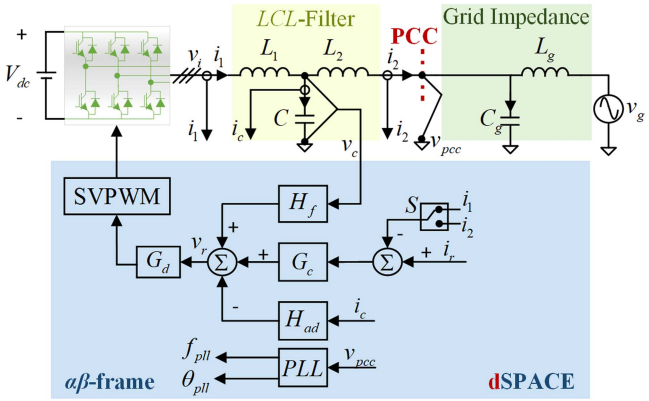

Fig. 1. Configuration of the studied three-phase GCI system with an *LCL* filter.

3) Experiments have been performed to demonstrate the effectiveness and superiority of the proposed design method in ensuring the stability and high performance of FARC-controlled *LCL*-type GCI against grid voltage distortions and grid impedance and frequency variations.

The rest of this article is organized as follows. Section II introduces the system configuration of the studied three-phase *LCL*-type GCI and the derivation of the corresponding admittance model. Section III gives the system stability conditions, analyzes the effect of grid frequency variation on the passivity of GCI's output admittance, and establishes and solves the optimization problem with passivity constraints. Experimental verification has been conducted in Section IV. Finally, Section V concludes this article.

II. System Configuration and Modeling of the LCL-Type GCI

Fig. 1 shows the configuration of the studied three-phase GCI system with an *LCL* filter. L_1, L_2, and C are the inverter-side inductor, grid-side inductor, and capacitor of the *LCL* filter, respectively. L_g and C_g stand for the transformer leakage inductor or transmission line inductor and power factor correction capacitor, respectively. i_1, i_2, i_c, v_i, v_c, $v_{\rm pcc}$, and v_g represent the inverter-side current, grid-side current, capacitor current, inverter output voltage, capacitor voltage, the voltage of point of common coupling (PCC), and grid voltage, and their uppercase symbols represent the corresponding s-domain variables.

The control algorithm is executed in the $\alpha\beta$-frame to eliminate the complexities associated with decoupling terms for *LCL*-filter topology in the dq-frame [32]. G_c is the current controller. $H_{\rm ad}$ and H_f represent the capacitor current feedback active damping (CCF-AD) controller and capacitor voltage feedforward active damping (CVF-AD) controller. Utilization of both CCF-AD and CVF-AD is for the passivity compliance design [33]. G_d stands for system delays, including sampling and pulsewidth modulation (PWM). Note that the selector $S = 1$ or 2 represents the ICC or GCC, respectively.

The per-phase control block diagram for the studied *LCL*-type GCI is drawn in Fig. 2, where the filter capacitor voltage v_c is regarded as the disturbance rather than the voltage at PCC used in

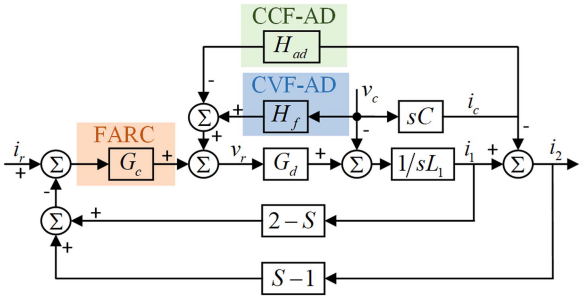

Fig. 2. Per-phase control block diagram for the studied *LCL*-type GCI.

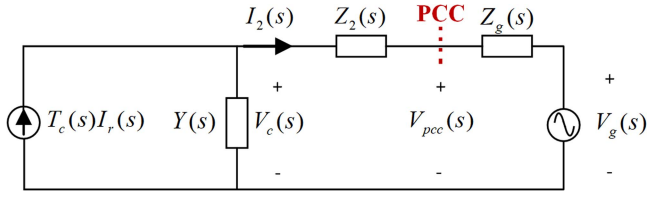

Fig. 3. Equivalent circuit for the *LCL*-type GCI.

most conventional modeling processes. This kind of derivation can result in a simpler control plant and GCI's output admittance model [33].

By applying Mason's formula to Fig. 2, the closed-loop transfer functions for the current reference i_r and filter capacitor voltage v_c to the grid current i_2 can, respectively, be derived as

$$T_c(s) = \left.\frac{I_2(s)}{I_r(s)}\right|_{V_c(s)=0} = \frac{G_c(s)G_d(s)}{L_1 s + G_c(s)G_d(s)} \tag{1}$$

and

$$Y(s) = -\left.\frac{I_2(s)}{V_c(s)}\right|_{I_r(s)=0} = \frac{1+L_1Cs^2+\{[(2-S)\cdot G_c(s)+H_{ad}(s)]\cdot Cs-H_f(s)\}G_d(s)}{L_1\cdot s + G_c(s)G_d(s)} \tag{2}$$

where $G_d(s) = e^{-Td\,s}$ and $T_d = 1.5T_s$.

Combing (1) and (2), the total grid current i_2 can be expressed as

$$I_2(s) = T_c(s)I_r(s) - Y(s)V_c(s). \tag{3}$$

Based on (3), the equivalent circuit can be obtained, as shown in Fig. 3, in which $Z_2(s) = L_2\,s$ and $Z_g(s)$ is the grid impedance.

III. Passivity-Compliance Control Parameters Design

A. Overall Closed-Loop System Stability Condition

According to Fig. 3, combining (3) with the equation $V_c(s) = V_g(s)+I_2(s)[Z_2(s)+Z_g(s)]$, the overall closed-loop current response can be expressed as

$$I_2(s) = I_r(s)\cdot\frac{T_c(s)}{1+[Z_2(s)+Z_g(s)]Y(s)} - V_g(s)\cdot\frac{Y(s)}{1+[Z_2(s)+Z_g(s)]Y(s)}. \tag{4}$$

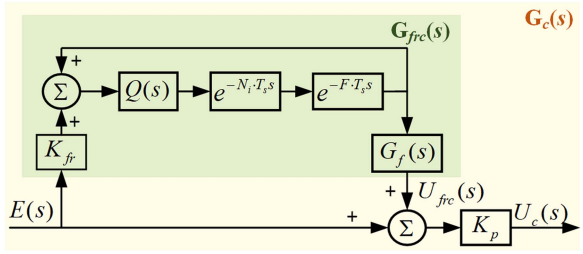

Fig. 4. Block diagram of the studied FARC.

From (4), it can be observed that the overall closed-loop system is stable if the following two conditions hold [22], [25].

1) *Internal stability:* The inner closed-loop system ($T_c(s)$) is asymptotic stable, which is recognized as independent of the grid impedance.
2) *External stability:* The roots of $1+[Z_2(s)+Z_g(s)]Y(s) = 0$ are all located in the left half of the s-plane, which reflects the interaction between the GCI's output impedance and the grid impedance.

In the derived system, ICC and GCC have identical inner closed-loop systems, and they can be easily tuned by introducing indexes of the open-loop system gain crossover frequency and the associated phase margin (PM) [22]. As for the second stability condition, if $[Z_2(s)+Z_g(s)]$ and $Y(s)$ are both passive, then the second stability condition is guaranteed. Assuming $[Z_2(s)+Z_g(s)]$ is a *RLC* network, it is passive. The remaining is to make $Y(s)$ passive [26].

B. Preselection of Controller Parameters for the Internal Stability

The controller parameters can be preselected via the transfer function-based frequency response method for the system's internal stability. Although this has already been well discussed in many papers [13], [14], [17], it is rearranged and briefed here for the integrality of the article.

The block diagram of FARC used in this article is depicted in Fig. 4. The transfer function of the current controller can be expressed as

$$G_c(s) = \frac{U_c(s)}{E(s)} = K_p[1+G_{frc}(s)] \tag{5}$$

where K_p is the proportional gain, and $G_{frc}(s)$ is the FARC with the following form:

$$G_{frc}(s) = \frac{U_{frc}(s)}{E(s)} = K_{fr}\frac{(e^{-N_iT_s s}\cdot e^{-FT_s s})Q(s)}{1-(e^{-N_iT_s s}\cdot e^{-FT_s s})Q(s)}G_f(s) \tag{6}$$

where K_{fr} is the FARC gain, and T_s is the control period. $G_f(s) = e^{mTs\,s}$ is the compensator that could be a pure leading element, and $Q(s) = a_1e^{Ts\,s}+a_0+a_1e^{-Ts\,s}$ with $2a_1+a_0 = 1$ is an LPF [13], [22]. N is the ratio of the sampling frequency and fundamental frequency of the grid, supposing $N = N_i + F$ with $N_i = \text{int}[N]$ being the integer part of N, and $F = N - N_i$ ($0<F<1$) being the fractional part of N, then $e^{-F\,Ts\,s}$ can be approximated by a

Lagrange interpolation-based FIR filter as follows [13]:

$$e^{-FT_s s} \approx \sum_{k=0}^{n} h(k) e^{-kT_s s} \tag{7}$$

where n is the order of the FIR filter. The coefficient can be obtained as

$$h(k) = \prod_{\substack{i=0 \\ i \neq k}}^{n} \frac{F-i}{k-i} \qquad k, i = 0, 1 \ldots n. \tag{8}$$

Substituting (7) into (6), giving

$$G_{frc}(s) = K_{fr} \frac{\left(e^{-N_i T_s s} \sum_{k=0}^{n} h(k) e^{-kT_s s}\right) Q(s)}{1 - \left(e^{-N_i T_s s} \sum_{k=0}^{n} h(k) e^{-kT_s s}\right) Q(s)} G_f(s). \tag{9}$$

1) Selection of the Proportional Gain K_p: Assuming $K_{fr} = 0$, the proportional gain K_p can be analytically designed according to the open-loop system gain at the crossover angular frequency and the associated PM [33]

$$K_p = \frac{\overbrace{\pi/2 - \varphi_m}^{\omega_c}}{T_d} L_1 \tag{10}$$

where φ_{m} is the desired PM, which is set to $\pi/3$ rad (60°) in this article. ω_c is crossover angular frequency.

2) Selection of m and K_{fr} for the FARC: Substituting (5) and (9) into (1), the inner closed-loop system transfer function $T_c(s)$ can be rewritten as

$$T_c(s) = \frac{T_{cp}(s)\left\{1 - Q(s)\left(e^{-N_i T_s s} \sum_{k=0}^{n} h(k) e^{-kT_s s}\right)\left[1 - K_{fr} G_f(s)\right]\right\}}{1 - Q(s)\left(e^{-N_i T_s s} \sum_{k=0}^{n} h(k) e^{-kT_s s}\right)\left[1 - K_{fr} G_f(s) T_{cp}(s)\right]} \tag{11}$$

where $T_{cp}(s) = T_{op}(s)/[1+T_{op}(s)]$ represent the inner closed-loop transfer function, and $T_{op}(s) = K_p G_d(s)/L_1 s$ represent the open-loop transfer function with only proportional control.

Since $T_{cp}(s)$ is asymptotically stable, $T_c(s)$ is stable if the following condition holds [34]:

$$\left\| Q(s) \sum_{k=0}^{n} \left(h(k) e^{-kT_s s}\right)\left[1 - K_{fr} G_f(s) T_{cp}(s)\right] \right\| \leq 1. \tag{12}$$

Choosing m and K_{fr} for the FARC is difficult since they are coupled in (12). Following the frequency-domain design approach in [35], (12) can be rewritten as

$$\begin{aligned} &\left\| 1 - K_{fr} N(\omega) e^{j[\theta(\omega) + m\omega T_s]} \right\| \leq \frac{1}{\|Q(j\omega)\|} \\ &\cdot \frac{1}{\left\| \sum_{k=0}^{n} \left(h(k) e^{-jkT_s \omega}\right) \right\|} \\ &= \frac{1}{a_0 + 2a_1 \cos(\omega T_s)} \cdot \frac{1}{\left\| \sum_{k=0}^{n} \left(h(k) e^{-jkT_s \omega}\right) \right\|}. \end{aligned} \tag{13}$$

Since $\left\| \sum_{k=0}^{n} \left(h(k) e^{-jkT_s \omega}\right) \right\| \leq 1$ is true, (13) always holds if

$$\left\| 1 - K_{fr} N(\omega) e^{j[\theta(\omega) + m\omega T_s]} \right\| \leq \frac{1}{a_0 + 2a_1 \cos(\omega T_s)}. \tag{14}$$

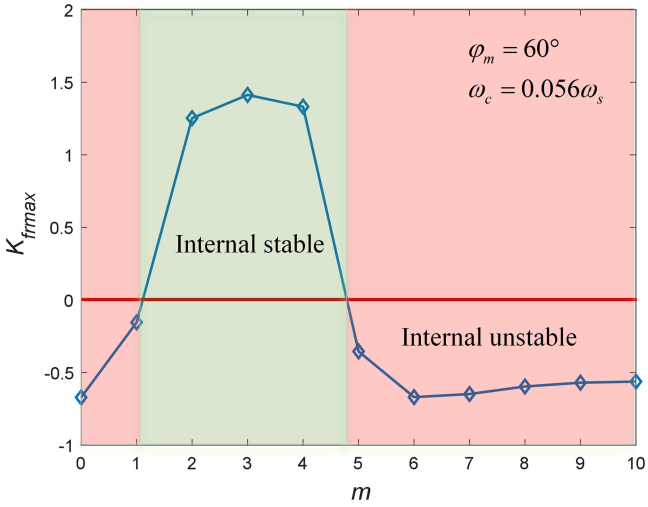

Fig. 5. Curve of $K_{fr\max}$ for different values of m ($a_1 = 0.25$ and $a_0 = 0.5$).

By using the Euler expansion, (14) can be further rewritten as

$$0 \leq K_{fr} \leq f(m, \omega) = \frac{a(\omega) + \sqrt{b(\omega)}}{N(\omega)} \tag{15}$$

where

$$\begin{aligned} a(\omega) &= \cos[\theta(\omega) + m\omega T_s] \\ b(\omega) &= \frac{1}{\left[a_0 + 2a_1 \cos(\omega T s)\right]^2} - \sin^2[\theta(\omega) + m\omega T_s] \\ N(\omega) &= \omega_c \Big/ \sqrt{\omega^2 + \omega_c^2 - 2\omega\omega_c \sin(\omega T_d)} \\ \theta(\omega) &= -\pi + \arctan \frac{\omega \cos(\omega T_d)}{\omega \sin(\omega T_d) - \omega_c}. \end{aligned}$$

Equation (15) holds if K_{fr} is smaller than the minima of the $f(m,\omega)$; thus, the upper boundary of K_{fr}, i.e., $K_{fr\max}$, is set to the minima of $f(m,\omega)$. For $K_{fr\max}$, the numerical results can be easily obtained using mathematical software, e.g., MATLAB. Fig. 5 shows the curve of $K_{fr\max}$ for different values of m. It can be seen that the value of m has a significant effect on the upper boundary of K_{fr}, so an appropriate value should be carefully selected for the system's internal stability. Note that all power stage parameters used in the analysis are given in Table II.

C. Passivity Compliance Design for the External Stability

1) Selection of Parameters for CCF-AD and CVF-AD: The external stability is guaranteed by carrying out the passivity compliance design for $Y(s)$, viz., making the real part of $Y(s)$ nonnegative. With only proportional control, the full-frequency nonnegative real part of $Y(s)$ can be achieved via the combination of proportional CCF-AD and CVF-AD. The parameter design guidelines for CCF-AD and CVF-AD in [33] are also briefed here for the integrality of the article.

CCF-AD feedback gains for ICC and GCC can be calculated according to

$$K_{ad} = (S-1)\omega_c L_1 - \frac{36\omega_c}{C\omega_s^2} \tag{16}$$

where $\omega_s = 2\pi/T_s$ is the sampling angular frequency.

In practice, the CVF-AD controller $H_f(s)$ consists of a band-pass filter (BPF) and a scaled first-order finite-impulse response LPF (FIR-LPF) as follows [33]:

$$\begin{aligned} H_f(s) &= K_f G_{\text{LPF}}(s) + K_{fb} G_{\text{BPF}}(s) \\ &= K_f \underbrace{\left(1 - a + ae^{-sT_s}\right)}_{G_{\text{LPF}}(s)} + K_{fb} \underbrace{\omega_{bc} \frac{s\cos\varphi_b - \omega_1 \sin\varphi_b}{s^2 + \omega_{bc}s + \omega_1^2}}_{G_{\text{BPF}}(s)} \end{aligned} \tag{17}$$

where K_f and a are the feedforward gain of CVF-AD and the parameter of FIR-LPF, respectively. Both of them are constants of less than one. K_{fb}, ω_1, ω_{bc}, and φ_b are the gain, fundamental angular frequency, cut-off angular frequency, and compensation angle of the BPF, respectively. ω_{bc} is set to $0.1\omega_1$. More details about parameter selection for CVF-AD can be found in [33].

2) Reselection of m and K_{fr} for Passivity Compliance: Ignoring the grid frequency variation, FARC degrades to RC. Following the method given in [22], the value of m can be further graphically optimized from the preselected values by using curves of the real part of the output admittance, enhancing the overall passivity of the output admittance as much as possible. Fig. 6 shows curves of the real part of the output admittance for different values of m associated with the corresponding maximum K_{fr} obtained from the previous Fig. 5. It can be seen from Fig. 6 that $m = 2$ is an optimal value for the ICC. In contrast, $m = 4$ is more appropriate for the GCC to achieve a relatively better overall passivity of the output admittance.

In consideration of the inversely proportional relationship between the gain of FARC and the passivity of output admittance, in other words, reducing the gain of FARC can drive the output admittance towards the passivity reinforcement. To this end, finding the upper boundary of K_{fr} becomes an optimization problem stated as follows:

$$\begin{aligned} \max \quad & K_{fr} \\ \text{s.t.} \quad & \min\{\text{Re}\{Y(j\omega)\}\} \geq 0, \omega \in \left(0, \frac{\omega_s}{2}\right) \\ & 0 < K_{fr} \leq K_{fr\max} \\ & f_g = f_{gn}. \end{aligned} \tag{18}$$

Solving the above optimization problem can obtain the upper boundary of K_{fr} for FARC at the nominal grid frequency, and the trivial trial and error method used in [22] is avoided. The flowchart for solving the proposed optimization problem is shown in Fig. 9, where the sweeping of grid frequency should be removed but fixed at the nominal one. In our studied case, the upper boundary of K_{fr} for internal stability is in accord with the passivity constraint for the ICC. In contrast, the upper boundary of K_{fr} must be reduced from 1.33 to 0.55 to fulfill the passivity constraint for the GCC. Fig. 7 shows curves of the real part of the output admittance when the gain of FARC is set to the upper boundary value. It can be seen that full-frequency passive output admittance is achieved at the nominal grid frequency f_{gn}, i.e., 50 Hz.

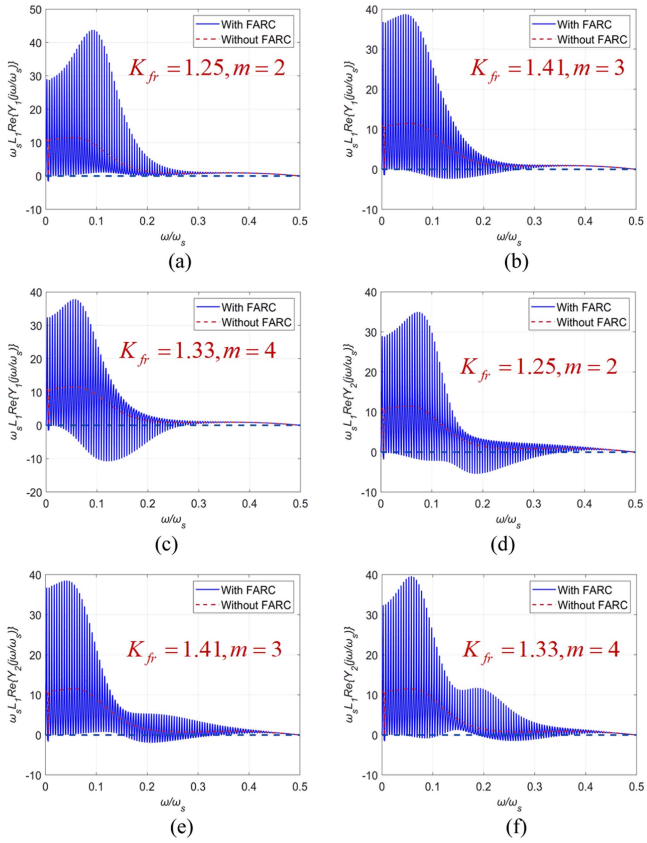

Fig. 6. Real part of the output admittance for different values of m associated with the corresponding maximum K_{fr}. (a) ICC with $m = 2$ and $K_{fr} = 1.25$. (b) ICC with $m = 3$ and $K_{fr} = 1.41$. (c) ICC with $m = 4$. and $K_{fr} = 1.33$. (d) GCC with $m = 2$ and $K_{fr} = 1.25$. (e) GCC with $m = 3$ and $K_{fr} = 1.41$. (f) GCC with $m = 4$ and $K_{fr} = 1.33$.

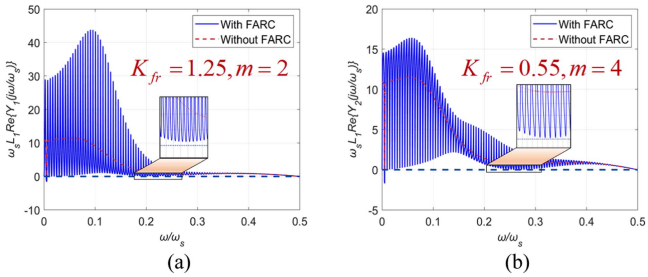

Fig. 7. Real part of the output admittance at the nominal grid frequency. (a) ICC with $m = 2$ and $K_{fr} = 1.25$. (b) GCC with $m = 4$ and $K_{fr} = 0.55$.

When considering the frequency adaptivity mechanism under the grid frequency variation, e.g., from $0.9\,f_{gn}$ to $1.1\,f_{gn}$, the minimum value for the real part of the output admittance varies along with the grid frequency (see Fig. 8, the minima is amplified 100 times and then projected in the yoz-plane with $x = 0.6$). For the ICC of our study case, the full-frequency passive output admittance is maintained in the presence of the grid frequency

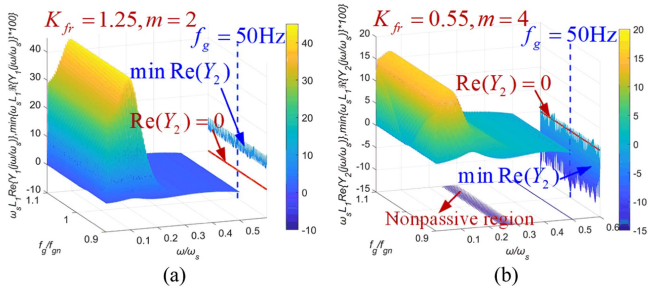

Fig. 8. Real part of the output admittance of either (a) ICC with $m = 2$ and $K_{fr} = 1.25$ or (b) GCC with $m = 4$ and $K_{fr} = 0.55$ in the presence of grid frequency varying from $0.9\,f_{gn}$ to $1.1\,f_{gn}$.

TABLE I
REFINED PARAMETERS FOR FARC CONCERNING PASSIVITY COMPLIANCE IN THE PRESENCE OF GRID FREQUENCY VARIATION

Type	m	K_{fr}
ICC	$m = 2$	$K_{fr} = K_{fr\max} = 1.25$
GCC	$m = 4$	$K_{fr} = 0.45$

variation, as shown in Fig. 8(a). In contrast, it is not the same for the GCC, where the negative real part of output admittance emerges as shown in Fig. 8(b)(the negative real part is projected in the *xoy*-plane with $z = -15$), which will jeopardize the passivity compliance that already obtained at the nominal grid frequency.

Taking into account the effect of grid frequency variation on passivity compliance for the GCI's output admittance, the constraint on the grid frequency of the optimization problem stated in (18) should be loosened from a single value of the nominal frequency to a certain range, which gives

$$\begin{aligned} \max \quad & K_{fr} \\ \text{s.t.} \quad & \min\{\mathrm{Re}\{Y(j\omega)\}\} \geq 0, \omega \in \left(0, \frac{\omega_s}{2}\right) \\ & 0 < K_{fr} \leq K_{fr\max} \\ & 0.9 f_{gn} \leq f_g \leq 1.1 f_{gn}. \end{aligned} \tag{19}$$

By solving the above new optimization problem, the upper boundary of K_{fr} for FARC concerning grid frequency variation can be obtained, which is given in Table I. The optimization problem established in this article can be solved offline in MATLAB with m-script. The flowchart for solving the proposed optimization problem is shown in Fig. 9. The solution of the proposed optimization problem provides an upper boundary value for the refined parameter K_{fr}. Fig. 10 shows curves of the real part of the output admittance with refined parameters for FARC. It can be seen that the full-frequency passive output admittance can be achieved in the presence of grid frequency varying from $0.9\,f_{gn}$ to $1.1\,f_{gn}$.

IV. EXPERIMENTAL VERIFICATIONS

Experiments have been conducted to verify the correctness of the theoretical stability analysis and the effectiveness of the

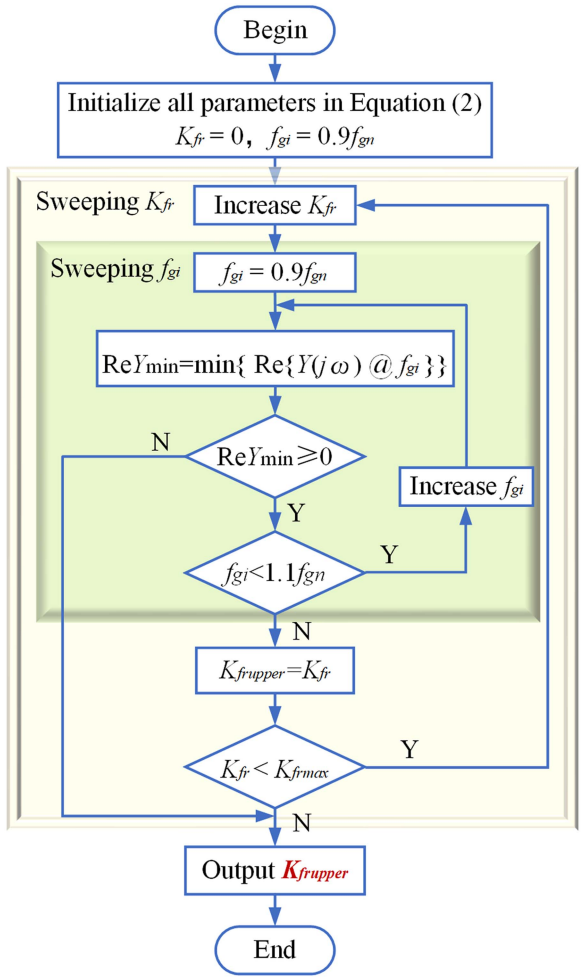

Fig. 9. Flowchart for solving the optimization problem.

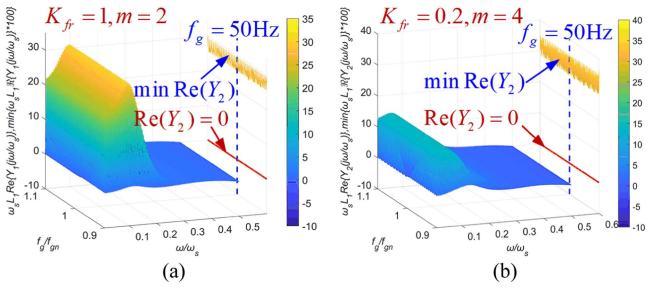

Fig. 10. Real part of the output admittance of either (a) ICC with $m = 2$ and $K_{fr} = 1$ or (b) GCC with $m = 4$ and $K_{fr} = 0.2$ in the presence of grid frequency varying from $0.9\,f_{gn}$ to $1.1\,f_{gn}$.

proposed controller parameter design method. The photo of the experimental setup is shown in Fig. 11. The setup consists of four three-phase Danfoss inverters with *LCL* filters, one of them serves as the GCI under test. The *LCL*-filter's parameters are given in Table II, and design rules can be found in [36]. In the test, a commercial grid emulator (IT7909) is used to generate background voltage harmonics and grid frequency variations. The designed control algorithm is implemented in the dSPACE

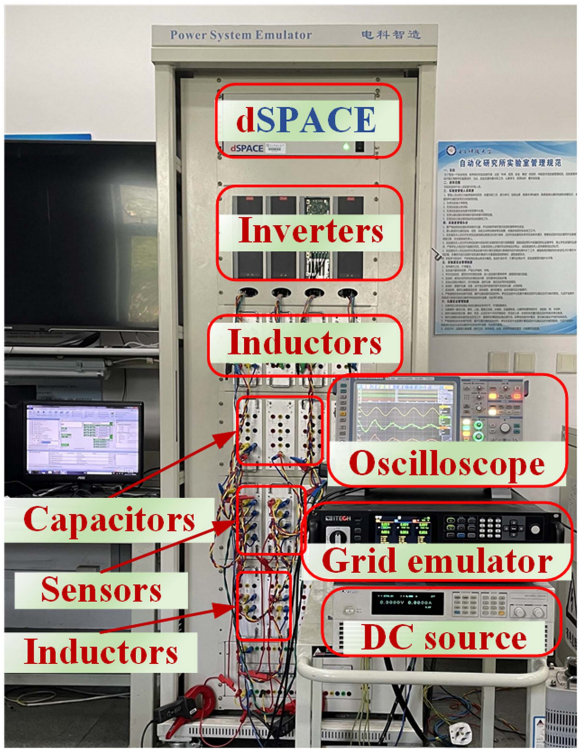

Fig. 11. Photograph of the experimental setup in the laboratory.

TABLE II
NOMINAL POWER STAGE PARAMETERS

	Symbol	Description	Value (p.u)
Inverter	V_{dc}	Input dc voltage	350 V (1)
	$S_{N.}$	Rated Power	1.4 kW (1)
	L_1	Inverter-side inductor	2.0 mH (0.024)
	L_2	Grid-side inductor	1.0 mH (0.012)
	C	Capacitor of *LCL*-filters	9.8 μF (12.53)
	f_s	Sampling and switching frequency	10 kHz (200)
	ω_s	Sampling angular frequency	62832 rad/s (200)
Grid	V_g	Grid voltage (Phase-to-ground RMS Voltage)	110 V (1)
	f_{gn}	Nominal grid frequency	50 Hz (1)
	L_g	Grid leakage inductors	8.0 mH (0.097)
	C_g	Grid capacitor	15 μF (8.19)

1005 platform for real-time control. The power stage parameters and controller parameters are given in Tables II and III, respectively.

A. External Stability Against Grid Frequency Variations

Before conducting experiments, theoretical stability assessments are performed by using Bode plots of both inverter output admittance and grid admittance. Normally, the stability in terms of PM can be interpreted by the phase difference at the intersection point of the magnitude responses of the GCI's output admittance and grid admittance [22], [25], viz., the phase difference over 180° indicates stability and vice versa. In the presence of the grid frequency variation, negative-real-part regions of the GCI's output admittance may appear, at which the intersection locations of the magnitude responses of the GCI's output admittance and grid admittance occurring may lead to system instability. In this article, the *LC*-type network is used to simulate the grid impedance (see Fig. 1) to build the instability conditions intentionally.

TABLE III
CONTROLLER PARAMETERS

	Symbol	Description	Value
Proportional Controller	K_p	Proportional gain	6.89 Ω
CCF-AD	K_{ad}	CCF gain for ICC	-3.25 Ω
	K_{ad}	CCF gain for GCC	3.73 Ω
CVF-AD	K_f	CVF gain	0.4 rad/s
	K_{fb}	BPF gain	0.6 rad/s^2
	a	Coefficient of FIR-LPF	0.5
	ω_{bc}	Cut-off angular frequency	31.4 rad/s
	φ_b	Phase compensation angle	0.078 rad

ICC mode with $m = 2$ and $K_{fr} = 1$ is tested at first. During the test, the grid frequency f_g changes from 50 to 54 Hz at a rate of 15 Hz/s. Experimental waveforms are given in Fig. 12, where the GCI operates normally, and no oscillations are observed even during the frequency transients process, as shown in Fig. 12(b). The experimental results are consistent with the theoretical expectation in Fig. 10(a) that the full-frequency passive output admittance is always fulfilled, even in the presence of the grid frequency variation.

The same tests are carried out for the GCC with $m = 4$ and $K_{fr} = 0.55$. Experimental waveforms are given in Fig. 13. The GCI operates normally at the nominal grid frequency. When the grid frequency changes from 50 to 54 Hz, the GCI's output current gradually oscillates, which respects the theoretical expectation in Fig. 8(b) that the negative of the GCI's output admittance emerges. According to the FFT analysis result, the oscillation frequency is around 2 kHz, which can be exactly predicted by the Bode plot given in Fig. 14.

Set K_{fr} to 0.2 for GCC, then perform the same tests. Experimental waveforms are given in Fig. 15. The GCI operates normally, and no oscillations are observed even during the frequency transients process, as shown in Fig. 15(b). The experimental results are in line with the theoretical expectation in Fig. 10(b) that the full-frequency passive output admittance is always fulfilled even in the presence of the grid frequency variation, and thus the system instability is prevented.

B. Current Quality Enhancement Against the Grid Voltage Distortion and Grid Frequency Variation

To show the superiority of the designed FARC in harmonics rejection and power quality enhancement in the presence of the grid voltage distortion and grid frequency variation, the grid emulator has added some low-order voltage harmonics (5th 3%, 7th 2.14%, 11th 1.36%, 13th 1.15%, 17th 0.88%, and THD is

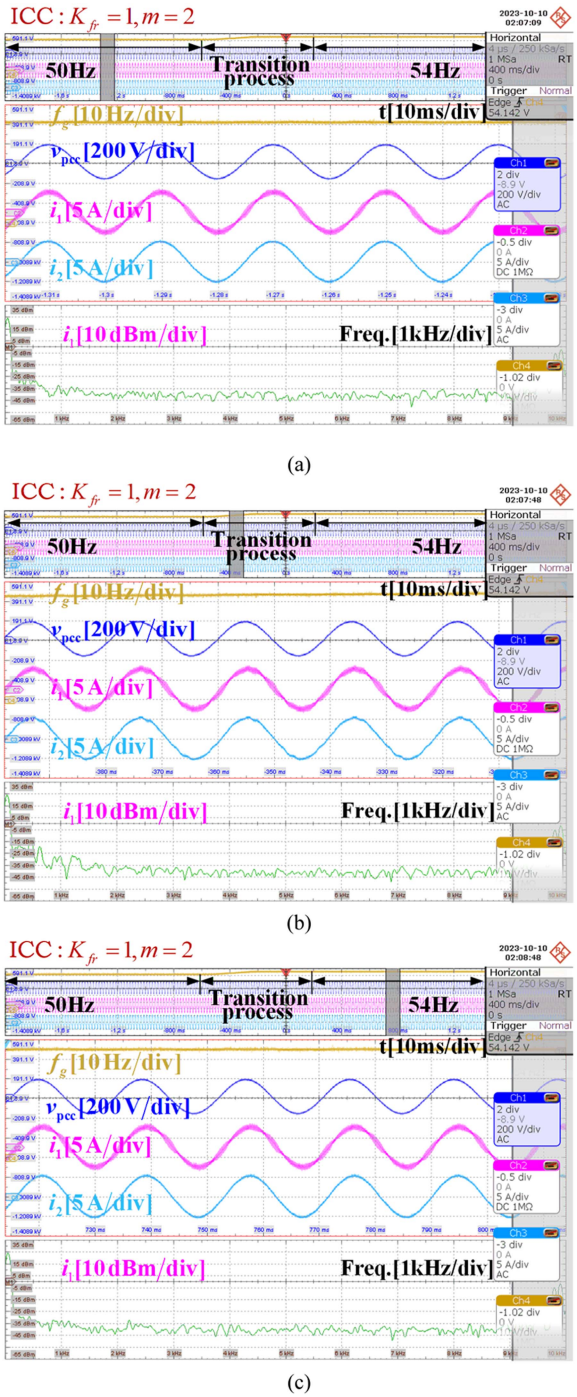

Fig. 12. Experimental waveforms of the ICC with $m = 2$ and $K_{fr} = 1$ in the presence of grid frequency f_g changes from 50 Hz to 54 Hz. (a) Steady-state 50 Hz. (b) Frequency transient process. (c) Steady-state 54 Hz.

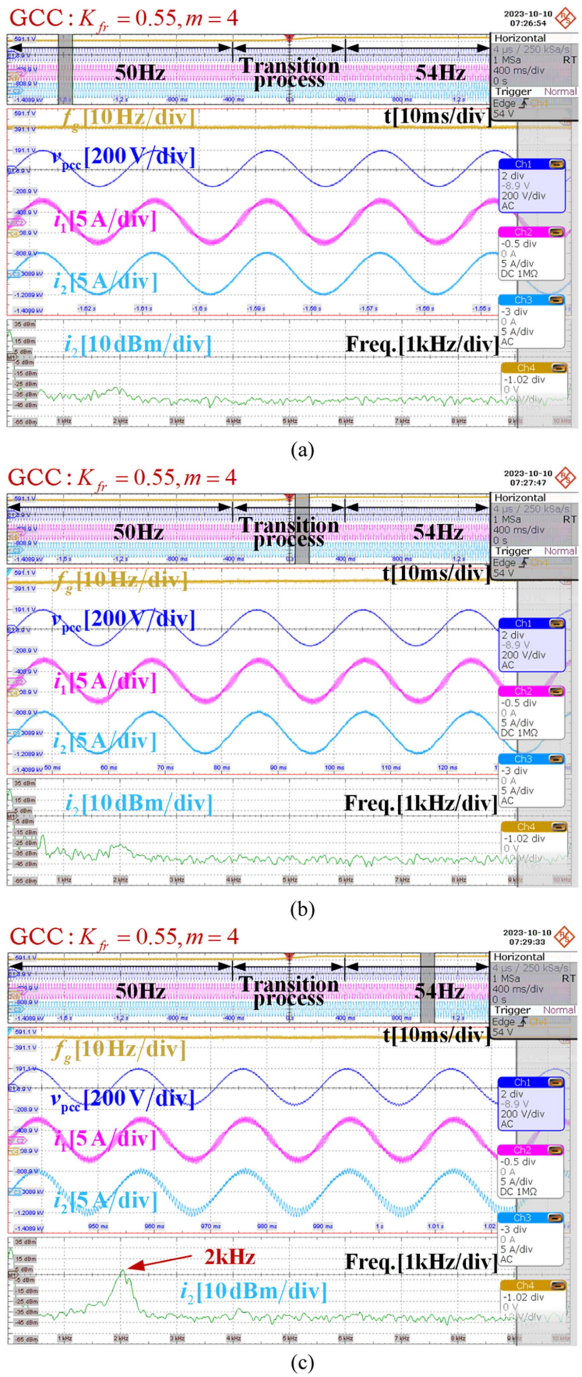

Fig. 13. Experimental waveforms of the GCC with $m = 4$ and $K_{fr} = 0.55$ in the presence of grid frequency f_g changes from 50 to 54 Hz. (a) Steady-state 50 Hz. (b) Frequency transient process. (c) Steady-state 54 Hz.

4.45%) for the test. During the test, the grid frequency f_g changes from 45 to 55 Hz at a rate of 15 Hz/s.

Experimental waveforms are given in Figs. 16 and 17, and the output current waveforms are always kept sinusoidal with THD less than 5%, which complies with the IEEE Std-1547 standard [37], even during the frequency transients process. Besides, the harmonic spectra of the controlled current are far below the standard. However, it's worth mentioning that the actual injection current to the grid is the grid-side current for the ICC and is highly distorted (THD = 5.55% and 5.88%) because current harmonics can freely flow into the filter capacitor of the *LCL*-filter. It's worth mentioning that during the grid frequency transient process, the harmonic spectra of the controlled current

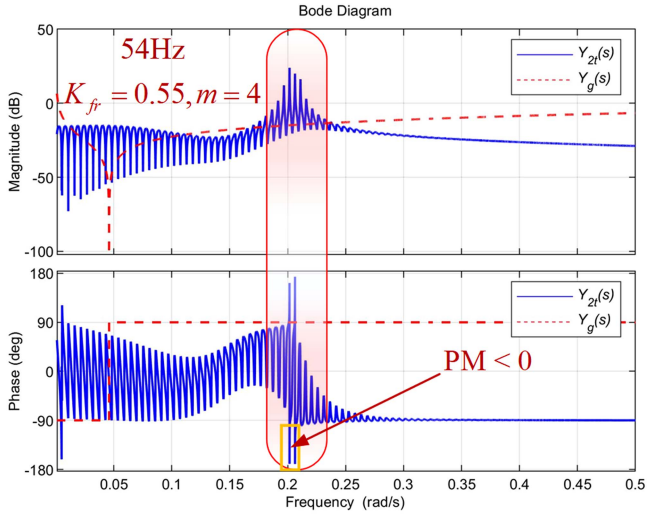

Fig. 14. Bode plots of $Y_{2t}(s)$ and $Y_g(s)$ for GCC with $m=4$ and $K_{fr}=0.55$.

TABLE IV
COMPARISON OF DIFFERENT STUDY CASES ON RC

Cases	Accuracy	Dynamic response	Frequency adaption	External stability
FARC+IIR [12]	High	Slow	Yes	Unknown
FARC+DB [18]	High	Slow	Yes	Unknown
PSRC [38]	High	Fast	No	Unknown
FAFRC [4]	High	Slow	Yes	Unknown
PBRC [22]	High	Slow	No	Yes
PBFARC	High	Slow	Yes	Yes

are also below the standard line for ICC mode while slightly over the standard line for GCC mode. The reason is that, compared with the GCC mode, the ICC mode has a larger feasible value for K_{fr} to meet the passivity constraint, which can render a faster system dynamic response.

With the FFT analysis, the curves of THD for output currents of ICC and GCC with different RCs in the presence of grid frequency variation are depicted in Fig. 18. For the conventional RC (CRC), without the frequency adaptivity mechanism, the performance severely degrades when the grid frequency bias the nominal value, which results in a sharp rising in THD of output current. Conversely, embedding with the frequency adaptivity mechanism to RC to construct the FARC, the output current's THD can always be maintained at a relatively low value below 5% against the wide grid frequency variation, which implies the necessity of adding the frequency adaptivity mechanism to CRC to sustain the high performance in the presence of grid frequency variation.

C. Discussion

Table IV gives some of the latest study cases in the field of RC design and applications to highlight the merit of the proposed one. A study case in [12] designed a FARC based on an improved IIR filter, which can effectively correct the resonant

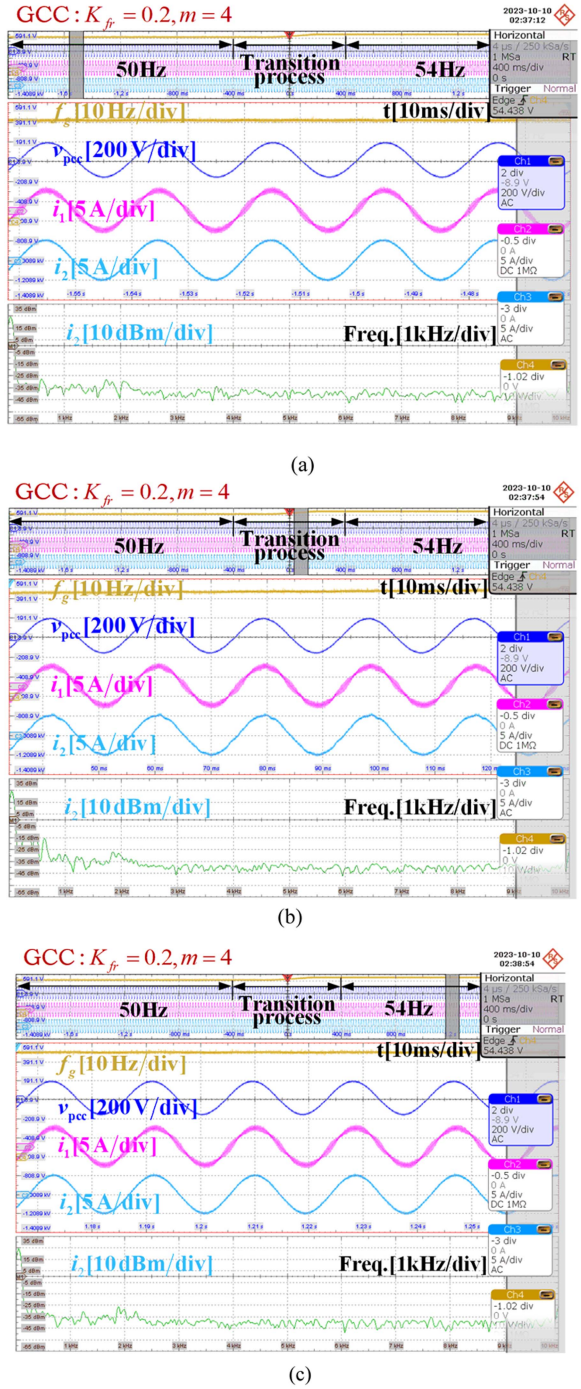

Fig. 15. Experimental waveforms of the GCC with $m=4$ and $K_{fr}=0.2$ in the presence of grid frequency f_g changes from 50 to 54 Hz. (a) Steady-state 50 Hz. (b) Frequency transient process. (c) Steady-state 54 Hz.

gain range of RC and ensure the tracking control accuracy when the frequency varies. The study case in [18] proposed a hybrid control scheme that combines a FARC controller with a deadbeat (DB) controller to obtain fast and accurate control in the presence of grid frequency variation and load changes. The study case in [38] introduces the parallel structure for the repetitive controller (PSRC). They have the advantage of fast dynamic response

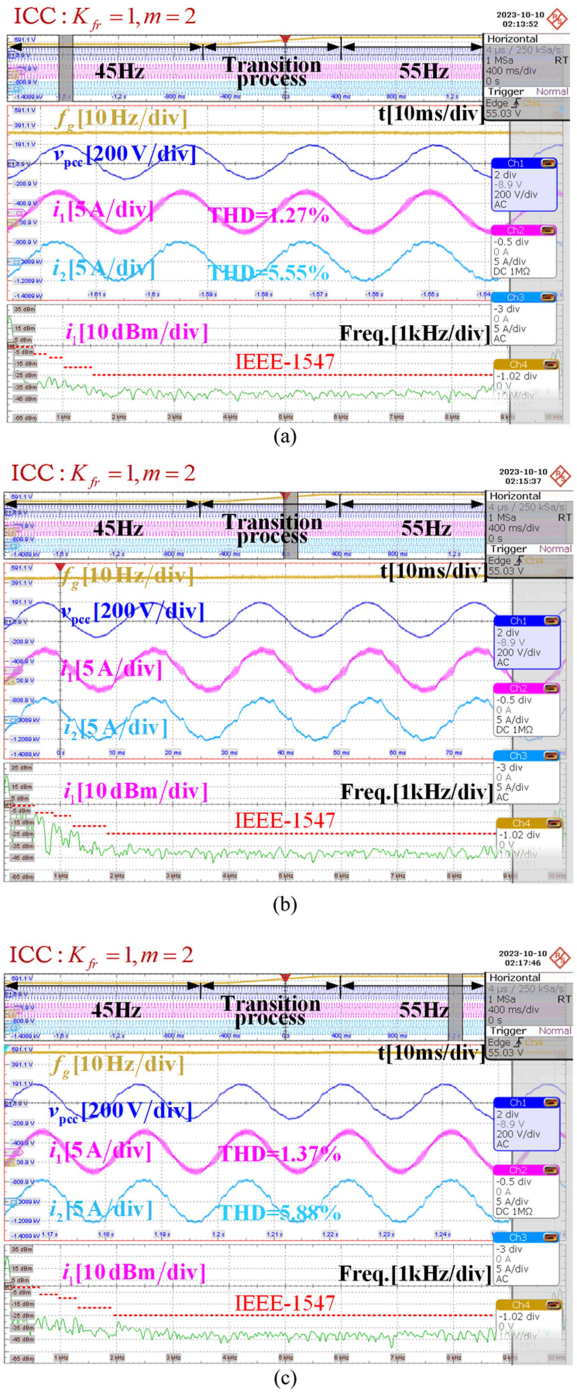

Fig. 16. Experimental waveforms of the ICC under distorted grid voltage and in the presence of grid frequency changes from 45 to 55 Hz. (a) Steady state 45 Hz. (b) Frequency transient process. (c) Steady-state 55 Hz.

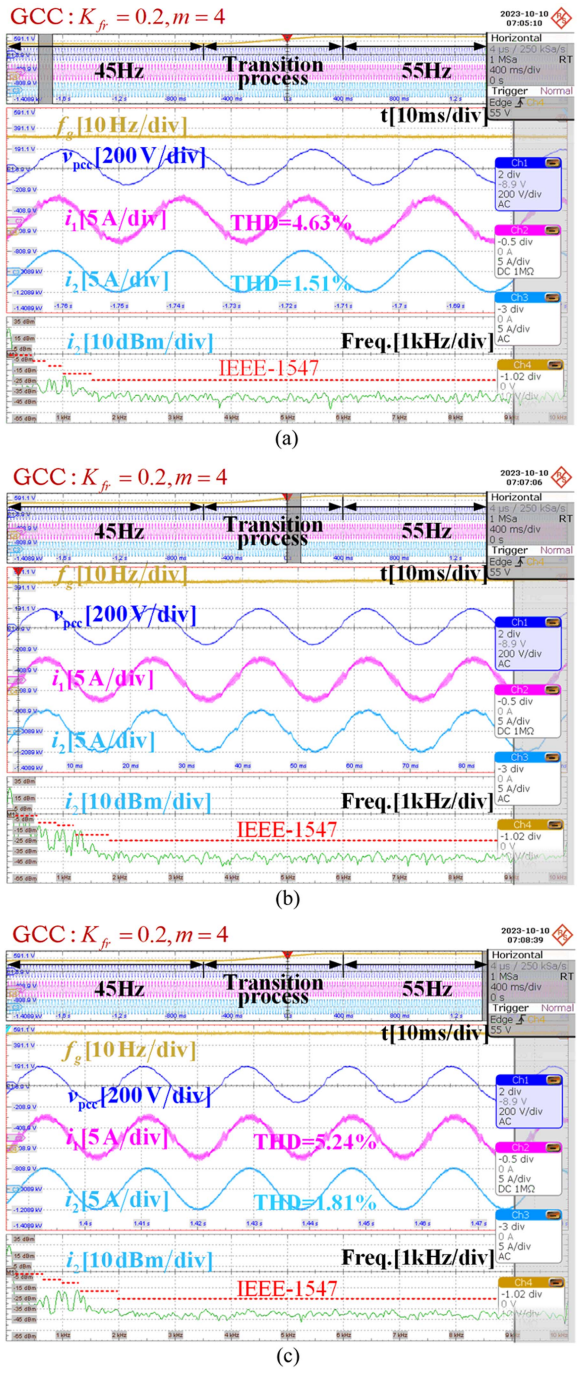

Fig. 17. Experimental waveforms of the GCC under distorted grid voltage and in the presence of grid frequency changes from 45 to 55 Hz. (a) Steady-state 45 Hz. (b) Frequency transient process. (c) Steady-state 55 Hz.

speed. Study case [4] proposed a novel frequency adaptive fast repetitive control (FAFRC) for APF with SiC-MOSFET inverter to achieve optimal performance in variable frequency girds through changing order N of RC.

The common drawback of the above study cases is that they are all designed on the basis of the system's closed-loop transfer function, which can only assess the internal stability of an individual GCI, and their external stability is unknown. Passivity-based RC is studied in [22] to guarantee the system's external stability. However, frequency adaptability is not considered. In this article, a stricter passivity constraint is imposed on the FARC design to guarantee the system's external stability in the presence of grid frequency variation. Sometimes, it will result in a sluggish dynamic response speed, such as for the GCC mode in the article.

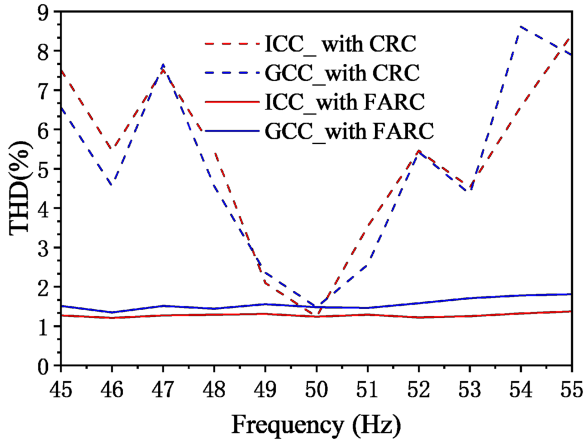

Fig. 18. Curves of THD for output currents of ICC and GCC with different RCs in the presence of grid frequency variation.

V. Conclusion

This article investigates the external stability issue of *LCL*-type GCIs with FARC from the perspective of output admittance's passivity. It finds that the frequency adaptive mechanism of FARC associated with the grid frequency variations may raise the negative conductance in the GCI's output admittance, which will jeopardize system stability. An optimization problem with constraints on internal stability, passivity compliance, and grid frequency variation is established to design the FARC parameters. The method is applicable for *LCL*-type GCIs with ICC or GCC structures to maintain the full-frequency passive output admittance against the grid frequency variation. Therefore, a sufficient stability condition and high control accuracy can be achieved simultaneously regardless of grid voltage distortion and grid impedance or frequency variations. Finally, experiments validate the theoretical findings.

The grid frequency variations and the frequency adaptive mechanism of FARC may also affect the system stability when applied to the island mode inverter, the study about this will be the future work.

References

[1] K. Zhou, C. Tang, Y. Chen, B. Zhang, and W. Lu, "A generic multi-frequency repetitive control scheme for power converters," *IEEE Trans. Ind. Electron.*, vol. 70, no. 12, pp. 12680–12688, Dec. 2023, doi: 10.1109/TIE.2023.3239855.

[2] Y. Yang et al., "A novel cascaded repetitive controller of an *LC* -filtered H6 voltage-source inverter," *IEEE J. Emerg. Sel. Top. Power Electron.*, vol. 11, no. 1, pp. 556–566, Feb. 2023, doi: 10.1109/JESTPE.2022.3212683.

[3] S. Jiang, D. Cao, Y. Li, J. Liu, and F. Z. Peng, "Low-THD, fast-transient, and cost-effective synchronous-frame repetitive controller for three-phase UPS inverters," *IEEE Trans. Power Electron.*, vol. 27, no. 6, pp. 2994–3005, Jun. 2012, doi: 10.1109/TPEL.2011.2178266.

[4] H. Lin, X. Guo, D. Chen, S. Wu, and G. Chen, "A frequency adaptive repetitive control for active power filter with 380V/75A SiC-inverter," *IEEE Trans. Ind. Appl.*, vol. 58, no. 4, pp. 5469–5479, Jul. 2022, doi: 10.1109/TIA.2022.3176848.

[5] J. Ye, L. Liu, J. Xu, and A. Shen, "Frequency adaptive proportional-repetitive control for grid-connected inverters," *IEEE Trans. Ind. Electron.*, vol. 68, no. 9, pp. 7965–7974, Sep. 2021, doi: 10.1109/TIE.2020.3016247.

[6] M. Zhu, Y. Ye, Y. Xiong, and Q. Zhao, "Multibandwidth repetitive control resisting frequency variation in grid-tied inverters," *IEEE J. Emerg. Sel. Top. Power Electron.*, vol. 10, no. 1, pp. 446–454, Feb. 2022, doi: 10.1109/JESTPE.2021.3077618.

[7] R. Teodorescu, M. Liserre, and P. Rodriguez, *Grid Converters For Photovoltaic and Wind Power Systems*. Hoboken, NJ, USA: Wiley, 2011.

[8] J. Sun, "Impedance-based stability criterion for grid-connected inverters," *IEEE Trans. Power Electron.*, vol. 26, no. 11, pp. 3075–3078, Nov. 2011, doi: 10.1109/TPEL.2011.2136439.

[9] M. A. Herrán, J. R. Fischer, S. A. González, M. G. Judewicz, I. Carugati, and D. O. Carrica, "Repetitive control with adaptive sampling frequency for wind power generation systems," *IEEE J. Emerg. Sel. Top. Power Electron.*, vol. 2, no. 1, pp. 58–69, Mar. 2014, doi: 10.1109/JESTPE.2013.2290572.

[10] E. Kurniawan, Z. Cao, and Z. Man, "Design of robust repetitive control with time-varying sampling periods," *IEEE Trans. Ind. Electron.*, vol. 61, no. 6, pp. 2834–2841, Jun. 2014, doi: 10.1109/TIE.2013.2276033.

[11] J. M. Olm, G. A. Ramos, and R. Costa-Castelló, "Stability analysis of digital repetitive control systems under time-varying sampling period," *IET Control Theory Appl*, vol. 5, no. 1, 2011, Art. no. 29, doi: 10.1049/iet-cta.2009.0308.

[12] P. Liu, C. Wang, Y. Zhang, Y. Liang, Y. Cui, and J. Fang, "Frequency adaptive repetitive control of new energy grid-connected inverter based on improved IIR," *IEEE Trans. Power Electron.*, vol. 38, no. 8, pp. 9539–9551, Aug. 2023, doi: 10.1109/TPEL.2023.3274185.

[13] Z. - X. Zou, K. Zhou, Z. Wang, and M. Cheng, "Frequency-adaptive fractional-order repetitive control of shunt active power filters," *IEEE Trans. Ind. Electron.*, vol. 62, no. 3, pp. 1659–1668, Mar. 2015, doi: 10.1109/TIE.2014.2363442.

[14] C. Xie, X. Zhao, M. Savaghebi, L. Meng, J. M. Guerrero, and J. C. Vasquez, "Multirate fractional-order repetitive control of shunt active power filter suitable for microgrid applications," *IEEE J. Emerg. Sel. Top. Power Electron.*, vol. 5, no. 2, pp. 809–819, Jun. 2017, doi: 10.1109/JESTPE.2016.2639552.

[15] D. Chen, J. Zhang, and Z. Qian, "An improved repetitive control scheme for grid-connected inverter with frequency-adaptive capability," *IEEE Trans. Ind. Electron.*, vol. 60, no. 2, pp. 814–823, Feb. 2013, doi: 10.1109/TIE.2012.2205364.

[16] P. Liu, C. Wang, Y. Zhang, Y. Cui, and J. Fang, "An improved repetitive control of grid-connected inverter," in *Proc. 4th Int. Conf. Power Energy Technol.*, 2022, pp. 1329–1333. doi: 10.1109/ICPET55165.2022.9918514.

[17] Z. Liu, B. Zhang, and K. Zhou, "Universal fractional-order design of linear phase lead compensation multirate repetitive control for PWM inverters," *IEEE Trans. Ind. Electron.*, vol. 64, no. 9, pp. 7132–7140, Sep. 2017, doi: 10.1109/TIE.2017.2686348.

[18] C. Tan, Q. Chen, L. Zhang, and K. Zhou, "Frequency-adaptive repetitive control for three-phase four-leg V2G inverters," *IEEE Trans. Transp. Electrific.*, vol. 7, no. 4, pp. 2095–2103, Apr. 2021, doi: 10.1109/TTE.2021.3063467.

[19] Z. Liu, B. Zhang, K. Zhou, and J. Wang, "Virtual variable sampling discrete Fourier transform based selective odd-order harmonic repetitive control of DC/AC converters," *IEEE Trans. Power Electron.*, vol. 33, no. 7, pp. 6444–6452, Jul. 2018, doi: 10.1109/TPEL.2017.2764020.

[20] Z. Liu, B. Zhang, K. Zhou, Y. Yang, and J. Wang, "Virtual variable sampling repetitive control of single-phase DC/AC PWM converters," *IEEE J. Emerg. Sel. Top. Power Electron.*, vol. 7, no. 3, pp. 1837–1845, Sep. 2019, doi: 10.1109/JESTPE.2018.2862411.

[21] Z. Liu, K. Zhou, Y. Yang, J. Wang, and B. Zhang, "Frequency-adaptive virtual variable sampling-based selective harmonic repetitive control of power inverters," *IEEE Trans. Ind. Electron.*, vol. 68, no. 11, pp. 11339–11347, Nov. 2021, doi: 10.1109/TIE.2020.3031452.

[22] C. Xie, D. Liu, K. Li, J. Zou, K. Zhou, and J. M. Guerrero, "Passivity-based design of repetitive controller for LCL-type grid-connected inverters suitable for microgrid applications," *IEEE Trans. Power Electron.*, vol. 36, no. 2, pp. 2420–2431, Feb. 2021, doi: 10.1109/TPEL.2020.3014365.

[23] M. Cespedes and J. Sun, "Impedance modeling and analysis of grid-connected voltage-source converters," *IEEE Trans. Power Electron.*, vol. 29, no. 3, pp. 1254–1261, Mar. 2014, doi: 10.1109/TPEL.2013.2262473.

[24] W. Liu, X. Xie, C. Yin, and X. Li, "Impedance model-based stability analysis of grid-connected converters under wide-range operating conditions," in *Proc. 16th IET Int. Conf. AC DC Power Transmiss.*, 2021, pp. 1236–1241. doi: 10.1049/icp.2020.0154.

[25] X. Wang, F. Blaabjerg, and P. C. Loh, "Passivity-based stability analysis and damping injection for multiparalleled VSCs with LCL filters," *IEEE Trans. Power Electron.*, vol. 32, no. 11, pp. 8922–8935, Nov. 2017, doi: 10.1109/TPEL.2017.2651948.

[26] L. Harnefors, L. Zhang, and M. Bongiorno, "Frequency-domain passivity-based current controller design," *IET Power Electron*, vol. 1, no. 4, 2008, Art. no. 455.
[27] A. Akhavan, H. R. Mohammadi, J. C. Vasquez, and J. M. Guerrero, "Passivity-based design of plug-and-play current-controlled grid-connected inverters," *IEEE Trans. Power Electron.*, vol. 35, no. 2, pp. 2135–2150, Feb. 2020, doi: 10.1109/TPEL.2019.2920843.
[28] C. Xie, K. Li, J. Zou, D. Liu, and J. M. Guerrero, "Passivity-based design of grid-side current-controlled LCL-type grid-connected inverters," *IEEE Trans. Power Electron.*, vol. 35, no. 9, pp. 9813–9823, Sep. 2020, doi: 10.1109/TPEL.2020.2971380.
[29] L. Harnefors, A. G. Yepes, A. Vidal, and J. Doval-Gandoy, "Passivity-based controller design of grid-connected VSCs for prevention of electrical resonance instability," *IEEE Trans. Ind. Electron.*, vol. 62, no. 2, pp. 702–710, Feb. 2015, doi: 10.1109/TIE.2014.2336632.
[30] S. Li and H. Lin, "Passivity enhancement-based general design of capacitor current active damping for LCL-type grid-tied inverter," *IEEE Trans. Power Electron.*, vol. 38, no. 7, pp. 8223–8236, Jul. 2023, doi: 10.1109/TPEL.2023.3265630.
[31] L. Harnefors, A. G. Yepes, A. Vidal, and J. Doval-Gandoy, "Passivity-based stabilization of resonant current controllers with consideration of time delay," *IEEE Trans. Power Electron.*, vol. 29, no. 12, pp. 6260–6263, Dec. 2014, doi: 10.1109/TPEL.2014.2328669.
[32] Y. Jia, J. Zhao, and X. Fu, "Direct grid current control of LCL-filtered grid-connected inverter mitigating grid voltage disturbance," *IEEE Trans. Power Electron.*, vol. 29, no. 3, pp. 1532–1541, Mar. 2014, doi: 10.1109/TPEL.2013.2264098.
[33] C. Xie, K. Li, J. Zou, and J. M. Guerrero, "Passivity-based stabilization of *LCL* -type grid-connected inverters via a general admittance model," *IEEE Trans. Power Electron.*, vol. 35, no. 6, pp. 6636–6648, Jun. 2020, doi: 10.1109/TPEL.2019.2955861.
[34] K. Zhou and D. Wang, "Digital repetitive controlled three-phase PWM rectifier," *IEEE Trans. Power Electron.*, vol. 18, no. 1, pp. 309–316, Jan. 2003, doi: 10.1109/TPEL.2002.807150.
[35] B. Zhang, D. Wang, K. Zhou, and Y. Wang, "Linear phase lead compensation repetitive control of a CVCF PWM inverter," *IEEE Trans. Ind. Electron.*, vol. 55, no. 4, pp. 1595–1602, Apr. 2008, doi: 10.1109/TIE.2008.917105.
[36] W. Tang, K. Ma, and Y. Song, "Critical damping ratio to ensure design efficiency and stability of *LCL* filters," *IEEE Trans. Power Electron.*, vol. 36, no. 1, pp. 315–325, Jan. 2021, doi: 10.1109/TPEL.2020.3000897.
[37] *IEEE Standard for Interconnection and Interoperability of Distributed Energy Resources with Associated Electric Power Systems Interfaces IEEE*, IEEE Std 1547-2018 Revis. IEEE Std 1547-2003, pp. 1–138, Apr. 2018, doi: 10.1109/IEEESTD.2018.8332112.
[38] W. Lu, K. Zhou, D. Wang, and M. Cheng, "A general parallel structure repetitive control scheme for multiphase DC–AC PWM converters," *IEEE Trans. Power Electron.*, vol. 28, no. 8, pp. 3980–3987, Aug. 2013, doi: 10.1109/TPEL.2012.2229395.

Ying Zhao received the B.S. degree in electrical engineering and automation from Southwest Minzu University, Chengdu, China, in 2021. She is currently working toward the M.S. degree in electronic information with the School of Automation Engineering, University of Electronic Science and Technology of China, Chengdu, China.

Her current research interests include modeling and control of grid-connected inverters for renewable energy generation.

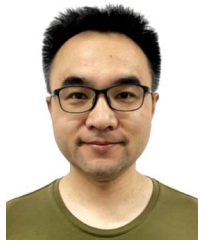

Chuan Xie (Senior Member, IEEE) received the B.S. degree in automation engineering from the University of Electronic Science and Technology of China (UESTC), Chengdu, China, and the Ph.D. degree in power electronics from Zhejiang University, Hangzhou, China, in 2007 and 2012, respectively.

Since 2012, he has been a Lecturer with the School of Automation Engineering, UESTC, where he was promoted to an Associate Professor in 2019. Since 2022, he has been a part-time Professor with Shenzhen Institute for Advanced Study, UESTC. From 2015 to 2016, he was a Visiting Scholar with the Department of Energy Technology, Aalborg University. His main research interests include digital control of power electronics, grid synchronization technology, distributed generation systems, microgrids and power quality.

Chao Peng received the M.S. and Ph.D. degrees in automation from the University of Electronic Science and Technology of China, Chengdu, China, in 2007 and 2012, respectively.

He is currently an Associate Professor with the School of Automation Engineering, Electronic Science and Technology of China, Chengdu. His research interests include renewable power generation system integration and control technologies.

Jianxiao Zou (Member, IEEE) received the B.S., M.S., and Ph.D. degrees in control science and engineering from the University of Electronic Science and Technology of China (UESTC), Chengdu, China in 2000, 2003, and 2009, respectively.

He is currently a Professor with UESTC, and has been serving as the Vice Dean with the Shenzhen Institute for Advanced Study, UESTC, since 2020. He was a Visiting Scholar with the University of California, Berkeley, CA, USA, in 2010; and a Senior Visiting Professor with Rutgers, the State University of New Jersey, New Brunswick, NJ, USA, in 2014. His research interests include control theory and control engineering, renewable energy control technologies, and intelligent information processing and control.